Check for updates

Stable oxygen reduction catalysts for enhancing rechargeability for zinc–air batteries: FeCoCu nanoparticles embedded in N-doped carbon matrices†

Wen Zhao,[a] Tianli Wu,*[b] Inosh Prabasha Perera,[c] Yanliu Dang,[d] Isaac T. Olowookere,[c] Qiang Luo, [c] Haiyan Tan,[d] Dilshan Silva[c] and Steven L. Suib *[acd]

Zinc–air batteries are potential devices for energy conversion and storage, offering high energy and power density. Efficient, durable, and cost-effective electrocatalysts that accelerate sluggish oxygen reduction kinetics are crucial for achieving high performance. Here we have developed a high-performance oxygen reduction catalyst based on N-doped carbon and FeCoCu particles encapsulated in graphitic carbon nanotube composites (N-doped carbon/FeCoCu). Through the systematic experimental and simulation studies, we propose a synergetic coupling among FeCoCu nanoparticles and N-doped carbon nanotubes. The electron transfer from FeCoCu nanoparticles to carbon active sites through metal−N−C moieties affects the crystal structure, local environment, and electronic properties of the catalyst, enhancing its conductivity, electrocatalytic performance, and reaction kinetics, while also providing exceptional durability in alkaline electrolyte. Consequently, as an alternative to the precious Pt catalyst, N-doped carbon/FeCoCu catalyst used in the air cathode of zinc–air batteries exhibits remarkable specific capacities (810 mA h g^{-1}) with large energy densities (918 W h kg^{-1}), and a peak power density of 154.7 mW cm^{-2}. Additionally, impressive reversibility and stability are demonstrated throughout extensive charge/discharge cycles over 900 h, holding great potential for practical applications in next-generation sustainable and green rechargeable batteries.

1. Introduction

As a clean power source device, metal-air batteries have gained ever-increasing attention in the energy storage field because of their remarkable theoretical energy density.[1–7] Among a variety of metals, zinc stands out for its safety, environmentally friendly characteristics, high theoretical energy density (1218 W h kg^{-1}), and cost-effectiveness.[8–13] Zinc–air battery (ZAB) systems are compatible with non-combustible aqueous electrolytes, effectively addressing safety and environmental concerns associated with the leakage of organic electrolytes in an open-cell configuration.[14] However, the efficiency of Zn–air batteries is impeded by sluggish kinetics and high overpotentials in the cathodic oxygen reactions, necessitating the use of electrocatalysts in the air cathode to catalyze both the oxygen reduction reaction (ORR) and the oxygen evolution reaction (OER).[15–18] Moreover, the limited rechargeability has been a challenge for zinc–air batteries, as the ORR catalyst tends to deactivate during the charging process at high voltage.[19] Thus, extensive efforts have been dedicated to the development of efficient, robust, and cost-effective ORR electrocatalysts, which can accelerate the electrochemical reaction kinetics at the air cathode while withstanding the alternating potentials during cycling.[20–22]

In an aqueous electrolyte, the oxygen reduction process involves the following steps: diffusion and adsorption of O_2 molecules at the surface of electrocatalysts, electron transport from the cathode to adsorbed O_2 molecules, weakening and splitting of O=O bonds, and release of the produced OH$^-$ ions into solution.[4,23] The overpotential of ORR can be assessed by analyzing the activation energy of the different elemental steps, directly correlated with the catalytic activity of the electrocatalyst. Conventional commercial electrocatalysts for the ORR include carbon-supported noble metal Pt (Pt/C) materials.[24,25] Despite their effectiveness, these Pt-based electrocatalysts face challenges such as high costs due to limited availability,

[a]Department of Materials Science and Engineering, University of Connecticut, 25 King Hill Rd Unit 3136, Storrs, Connecticut 06269-3136, USA. E-mail: steven.suib@uconn.edu

[b]Henan Key Laboratory of Quantum Materials and Quantum Energy, School of Future Technology, Henan University, Kaifeng 475004, China. E-mail: tianliwu@henu.edu.cn

[c]Department of Chemistry, University of Connecticut, 55 N. Eagleville Rd., Storrs, Connecticut 06269-3060, USA

[d]Institute of Materials Science, University of Connecticut, 25 King Hill Rd Unit 3136, Storrs, Connecticut 06269-3136, USA

† Electronic supplementary information (ESI) available. See DOI: https://doi.org/10.1039/d5ta00482a

susceptibility to fuel crossover, and poor stability, significantly hindering their widespread commercialization.[5,26] Numerous studies have verified metal-based nitrogen-doped carbon materials as promising substitutes for Pt-based catalysts.[15,20,27–33] The electrocatalytic activities of various carbon materials, including graphene, carbon black, carbon nanotubes (CNTs), or activated carbon, can be significantly enhanced by introducing heteroatoms such as nitrogen.[34–38] Additionally, with a porous structure and outstanding electrical conductivity, carbon materials can serve as both the support for electrocatalysts and the current collector, promoting ion diffusion and facilitating electron transfer.[39,40] Modifying the electronic structure of active centers is a powerful strategy to enhance catalytic properties.[28] Transition metals (M = Mn, Fe, Co, Ni, Cu) have available 3d unoccupied orbitals can effectively modify the local electronic structure of carbon matrix via electron transfer, thereby optimizing the adsorption/desorption of oxygen-containing intermediates.[41–43] Consequently, metal-based nitrogen-doped carbon catalysts demonstrate high conductivity and unique metal–ligand interactions, which contribute to their exceptional performance in oxygen activation.[44,45] Plenty of transition metals (Fe, Co, Ni) have been widely explored for ORR/OER electrocatalysts and recent research shows that bimetallic or multi-metallic particles outperform their monometallic counterparts among non-noble metal-based nitrogen-doped carbon electrocatalysts.[5,40,46,47] For instance, studies focusing on the atomically dispersed Co–Fe system reveal that synergetic effects between $Fe-N_4$ and $Co-N_4$ enhanced ORR activity.[48,49] Other research suggests that the strong electronic coupling between FeCo, FeCoNi alloy particles with carbon materials makes alloy particle-embedded N-doped carbon materials promising candidates for ORR catalysis.[5,40] Cu with high electron density in d orbits can act as electron donor to adjust the electronic structure of active sites for ORR but the research on ternary FeCoCu/carbon catalysts is limited.[50] In addition, the comprehensive understanding of the interaction and synergistic effects of transition metals in metal-based nitrogen-doped carbon materials and their impact on catalytic ORR performance remains obscured. Therefore, it is of great importance to improve the catalytic activity by optimizing metal species and employing a systematic design to explore the catalytic mechanisms.

Here, we developed a catalyst composed of FeCoCu particles encapsulated and supported on nitrogen-doped carbon. The formation of this ternary N-doped carbon/FeCoCu electrocatalyst involves the introduction of Cu metal into the conventional N-doped carbon/FeCo system through pyrolysis and carbonization processes. Because of their high inherent electrocatalytic activity, hierarchically porous structures promoting efficient mass transport, and large specific surface area offering abundant active sites, N-doped carbon/FeCoCu-15 systems exhibit superior ORR performance in alkaline media. Specifically, N-doped carbon/FeCoCu catalysts exhibits a positive half-wave potential ($E_{1/2}$) of 0.852 V vs. reversible hydrogen electrode (RHE), a high kinetic current density (J_k) of 16.44 mV cm^{-2} at 0.85 V, and a Tafel slope of 61.6 mV dec^{-1}, surpassing commercial Pt/C catalysts. Density functional theory (DFT)

calculations reveal that the high efficiency and rapid kinetics of N-doped carbon/FeCoCu-15 are attributed to the electron-donating characteristics of FeCoCu nanoparticles and nitrogen doping in the carbon matrix, which not only improve electronic conductivity but also create a favorable surface electronic environment, thereby enhancing ORR performance. Furthermore, N-doped carbon/FeCoCu demonstrates remarkable performance in aqueous rechargeable zinc–air batteries, achieving a near-theoretical specific capacity of 810 mA h g^{-1} with an energy density of 918 W h kg^{-1} and exhibiting exceptional durability for more than 900 hours of cycling.

2. Experimental

All reagents used in this work were of analytical grade and were used without further purification: zinc chloride ($ZnCl_2$, Sigma-Aldrich), iron(ii) chloride tetrahydrate ($FeCl_2 \cdot 4H_2O$, Sigma-Aldrich), cobalt(ii) chloride hexahydrate ($CoCl_2 \cdot 6H_2O$, Sigma-Aldrich), copper(ii) chloride ($CuCl_2$, Sigma-Aldrich), form-amide (Fisher Scientific), potassium hydroxide (KOH, Sigma-Aldrich), 20% Pt/C (20% Pt on graphite, Sigma-Aldrich), Nafion solution (D-521, 5 wt% in water and 1-propanol, Fisher Scientific). Zinc foil (0.025 cm thickness, Alfa Aesar) was cleaned with water and ethanol. Toray carbon paper (30% wet proofing) was purchased from Fuel Cell Earth. Carbon cloth as a gas diffusion layer was purchased from MTI Corporation.

2.1 Catalysts preparation

For a typical synthesis of formamide-converted N-doped carbon materials decorated with FeCoCu particles (referred to as N-doped carbon/FeCoCu-15), the following procedure was followed.[46] First, specific quantities of $ZnCl_2$, $FeCl_2$, $CoCl_2$, and $CuCl_2$ were dissolved in formamide, resulting in a Zn/Fe/Co/Cu solution with concentrations of 0.088, 0.006, 0.006, and 0.015 mol L^{-1}, respectively. Subsequently, 40.0 mL of the Zn/Fe/Co/Cu salt formamide solution was sealed in a 100 mL Teflon-lined autoclave, which was heated to 190 °C and maintained at this temperature for 6 hours. After the reaction, a black precipitate was obtained and separated via centrifugation. The separated precipitate was then subjected to carbonization at 900 °C for 1 hour under a nitrogen (N_2) atmosphere with a gas flow rate of 50 cc min^{-1}. A black product was obtained once the tube furnace had cooled down to room temperature. The resulting product was directly used as a catalyst without any additional treatment. To examine the effect of composition on ORR performance, N-doped carbon/FeCo (without the addition of a Cu precursor) and N-doped carbon/FeCoCu materials with varying Cu content, ranging from 2 mmol to 20 mmol, were prepared using the same procedures.

2.2 Materials characterization

The phases and crystalline structures of the as-prepared samples were determined by X-ray diffraction (XRD) using a Rigaku SmartLab multipurpose X-ray diffractometer with Cu Kα radiation ($\lambda = 0.154$ nm). Surface chemistry was analyzed using X-ray photoelectron spectroscopy (XPS) on a PHI Model

This journal is © The Royal Society of Chemistry 2025

J. Mater. Chem. A, 2025, 13, 14216–14228 | 14217

590 spectrometer with an Al Kα source and all binding energies were referenced to the C 1s peak (284.8 eV). The specific surface area and pore size distribution of catalysts were analyzed using N_2 adsorption–desorption measurements based on the Brunauer–Emmett–Teller (BET) method on a Quantachrome Autosorb-1-1C automated adsorption system. Raman spectra were collected using a Renishaw 2000 Ramascope Micro-Raman coupled with a 514 nm Ar ion laser. Nuclear magnetic resonance (NMR) spectra were acquired on a Bruker Avance III 400 WB with a 4 mm HXY probe tuned for ^{59}Co (94.9 MHz). The microscopic morphology and microstructure of the samples were investigated via scanning electron microscopy (SEM) and transmission electron microscopy (TEM). SEM was performed using a Verios 4 L at an accelerating voltage of 2 kV under the immersion mode. High-resolution TEM and elemental mappings were collected on a Talos 200 S/TEM with electron acceleration energy of 200 kV. High-angle annular dark-field scanning transmission electron microscopy (HADD-STEM) were conducted using a Titan Themis AC-STEM equipped with a probe-spherical aberration corrector and a SuperX silicon drift detector energy-dispersive X-ray spectrometry (EDXS) system, operating at an accelerating voltage of 300 kV.

2.3   Electrochemical measurement

To evaluate electrocatalytical performance of the as-prepared catalysts, rotation disk electrode (RDE) measurements were performed on a CHI 760E electrochemical workstation (CH Instruments, Inc., Shanghai) using a three-electrode configuration. To prepare a homogeneous dispersion, 5 mg of synthesized active materials or 20% Pt/C and 10 µL of Nafion solution (5%) were dispersed in a 500 µL mixture of water and isopropanol with a volume ratio of 4 : 1. The suspension was ultrasonicated for 30 minutes, and then 10 µL of the homogeneous suspension was dropped onto a polished graphite rotation electrode with a surface area of 0.159 cm^2 and allowed to dry in ambient air. The resulting electrode was employed as the working electrode, with a graphite rod serving as the counter electrode and Hg/HgO as the reference electrode. The reference electrode was calibrated against a reversible hydrogen electrode in a hydrogen-saturated solution, with two Pt wires utilized as the working and counter electrodes. The thermodynamic potential for the hydrogen electrode reaction was determined as the average of potentials at which the current crossed zero (Fig. S1†). The ORR performance of the catalysts was investigated by cyclic voltammetry (CV) at a scan rate of 20 mV s^{-1} and linear sweep voltammetry (LSV) at a scan rate of 10 mV s^{-1} in an N_2- and O_2-saturated 0.1 M KOH solution, while varying the disk rotation rate at 400, 800, 1200, 1600, 2000, and 2500 rpm. A chronoamperometry measurements at 0.45 V vs. RHE were carried out to evaluate durability. The electrochemically active surface area (ECSA) of catalyst is estimated from electrochemical double-layer capacitance (C_{dl}), which is obtained by measuring CVs at different scan rates in the non-faradaic potential range in 0.1 M KOH. Electrochemical impedance spectroscopy (EIS) was recorded at 0.4 V vs. RHE for ORR in the frequency range of 0.1 Hz to 100 kHz. For the OER tests, measurements were conducted in 1.0 M KOH electrolyte at room temperature. LSV was recorded at a scan rate of 10 mV s^{-1}, with the disk rotation rate set to 1600 rpm to determine the overpotential at 10 mA cm^{-2}. All the potentials reported in this work were referenced to the RHE. Detailed calculations and analysis are given in ESI.†

Rechargeable zinc–air battery measurements were conducted with coin cells and home-built two-electrode flow batteries, utilizing an MTI battery analyzer (model BST8-300-CST). Zinc–air coin cells were assembled using a zinc plate as the anode, and an air electrode with electrocatalysts coated on carbon paper. The electrolyte consists of mixed solutions containing 0.2 M $ZnCl_2$ and various concentrations of KOH. The air cathodes were formulated by combining 20 mg of synthesized ORR catalysts (or 10 mg of synthesized catalysts plus 10 mg of RuO_2) and 100 µL of 5% Nafion solution into a 900 µL mixture of water and isopropanol with a volume ratio of 4 : 1. After ultrasonication for 30 minutes, the resulting mixture was applied onto carbon paper using a film applicator, achieving a catalyst loading of 1.3 mg cm^{-2}. Flow batteries were constructed with a Zn plate serving as the anode and electrocatalysts coated on carbon cloth as the air cathode. A circulating solution of 6 M KOH and 0.2 M $ZnCl_2$ was employed, with an external pump facilitating fluid flow through the cell. To prepare a homogenous ink solution,10 mg of ORR catalyst (synthesized active materials or 20% Pt/C), 10 mg of a commercial OER catalyst (RuO_2), and 100 µL of Nafion solution (5%) were dispersed in a 900 µL mixture of water and isopropanol with a volume ratio of 4 : 1. The suspension underwent ultrasonication for 30 minutes. Subsequently, 200 µL of the homogeneous suspension was applied to a 2×2 cm^2 carbon cloth gas diffusion layer. The active loading for both the ORR and OER catalysts was 0.5 mg cm^{-2}.

2.4   Computational details

All theoretical calculations were performed with the Vienna Ab initio Simulation Package (VASP), which implemented projector augmented wave pseudo-potentials (PAW) to describe the interaction between nuclei and electrons with density functional theory (DFT).[51] The cut-off energy for plane wave is set to 500 eV. The energy criterion is set to 10^{-5} eV in iterative solution of the Kohn–Sham equation. The Brillouin zone integration is performed using a $5 \times 5 \times 5$ k-mesh. All the structures are relaxed until the residual forces on the atoms have declined to less than 0.01 eV $Å^{-1}$.

3.   Results and discussion

3.1   Materials characterization

The N-doped carbon/FeCo and N-doped carbon/FeCoCu samples were synthesized via a hydrothermal and carbonization strategy. To determine the optimum compositions for the trinary N-doped carbon/FeCoCu system, samples with different ratios of Cu were examined. SEM images (Fig. S2†) display similar carbon morphologies for N-doped carbon/FeCo and N-doped carbon/FeCoCu materials. Further insights into the

14218 | J. Mater. Chem. A, 2025, 13, 14216–14228

This journal is © The Royal Society of Chemistry 2025

detailed structure of these samples are provided by TEM images (Fig. S3†). N-doped carbon/FeCo and N-doped carbon/FeCoCu-15 composites display a morphology combining carbon nanosheets and metal nanoparticles encapsulated in carbon nanotubes. In contrast, N-doped carbon/FeCoCu-2 and N-doped carbon/FeCoCu-10 show no evidence of metal particles or carbon nanotubes, while N-doped carbon/FeCoCu-20 presents large metal particles embedded in carbon nanosheets instead of carbon nanotubes. HRTEM images of N-doped carbon/FeCo (Fig. 1a) and N-doped carbon/FeCoCu-15 (Fig. 1c) display an intricate nanotube structure with metal nanoparticles wrapped inside. During the hydrothermal reaction at 190 °C, the organic solvent formamide undergoes thermal decomposition, while transition metal salts react to form a high nitrogen-content carbon precursor, M_x-$(CHN)_n$-Zn_y.[52] During the carbonization process, the metal precursors were reduced by pyrolysis

intermediates, leading to the formation of metal nanoparticles. Transition metals such as Fe, Co, Ni, and Cu catalyze CNTs growth by facilitating the bonding of planar CHN precursor atoms to the surface of the metal nanoparticles, which lowers the energy barrier and promotes the formation of graphitic carbon nanotubes with an inner diameter corresponding to that of the metal particles.[53] As the carbon nanotubes grew and clusters of alloy particles were embedded within them, a structure with bamboo-like morphology and abundant cavities formed.[8,46] With the incorporation of Cu, both the metal particles and carbon nanotubes demonstrate increased sizes compared to those in N-doped carbon/FeCo. Within N-doped carbon/FeCo, the binary FeCo alloy particles have an average diameter of approximately 50 nm (Fig. 1b). The selective area electron diffraction (SAED) pattern (inset of Fig. 1b) demonstrates a primitive cubic structure with an interplanar spacing
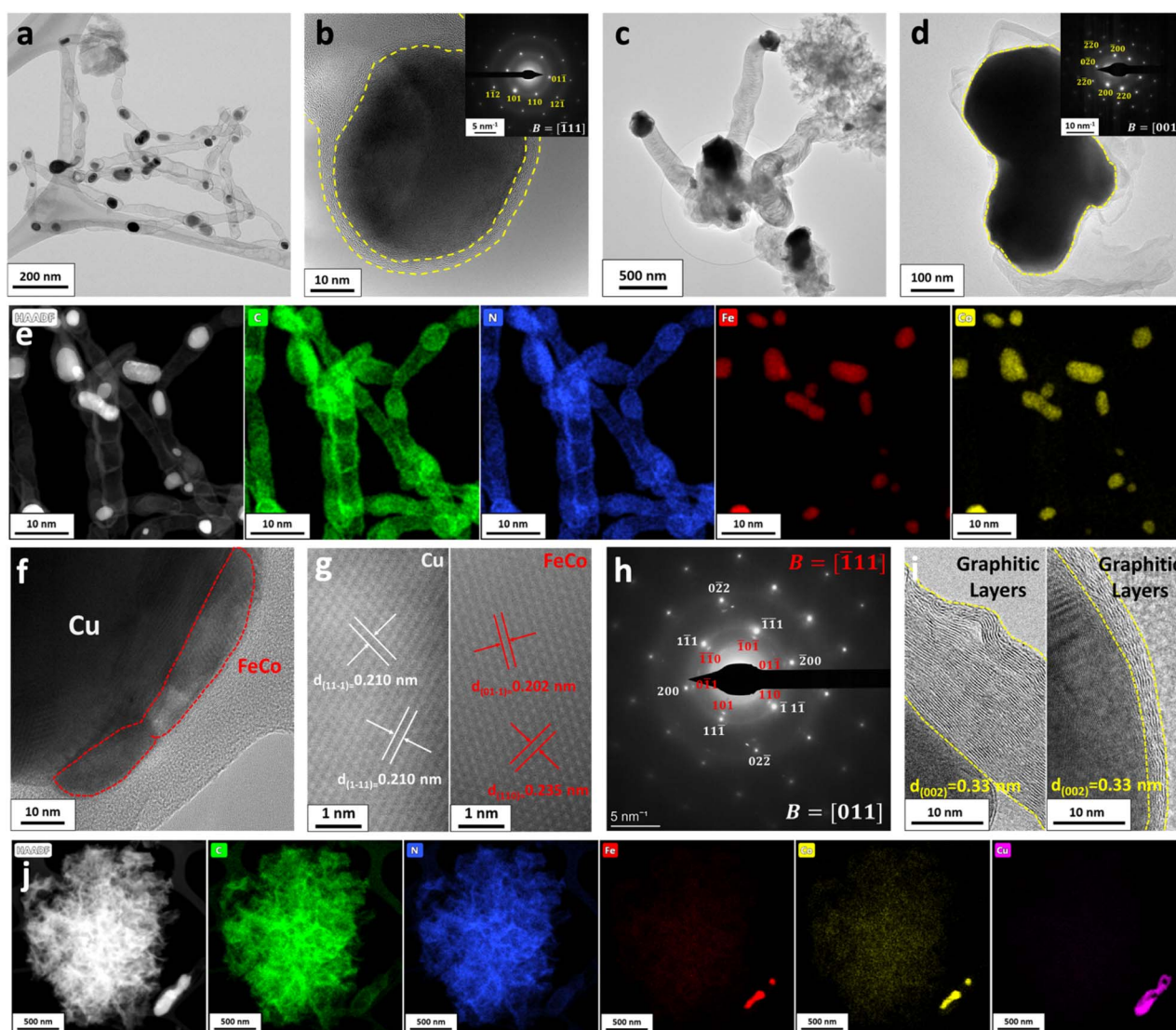

Fig. 1   (a and b) TEM images of N-doped carbon–FeCo. (c and d) TEM images of N-doped carbon/FeCoCu-15. (e) HAADF–STEM image and corresponding EDS elemental mappings of N-doped carbon/FeCo. (f) TEM image, (g) high-resolution HAADF–STEM images, and (h) SAED patterns of the Cu/FeCo boundary. (i) TEM images of graphitic nanotubes in N-doped carbon/FeCo (left) and N-doped carbon/FeCoCu-15 (right). (j) HAADF–STEM image and corresponding EDS elemental mappings of N-doped carbon/FeCoCu-15.

of 0.202 nm, corresponding to the (110) facets of the FeCo alloy. On the contrary, as illustrated in Fig. 1d, N-doped carbon/FeCoCu-15 displays larger metal particles, with dimensions approximately 300×500 nm. The face-centered cubic structure in the SAED pattern (inset of Fig. 1d) is identified to be Cu metal. The elemental distribution in N-doped carbon/FeCo and N-doped/FeCoCu samples was characterized using high-angle annular dark-filed scanning TEM (HAADF–STEM) and energy-dispersive spectroscopy (EDS) mappings. As shown in Fig. 1e, nitrogen is effectively incorporated into carbonaceous nanotubes in N-doped carbon/FeCo, with Fe and Co species co-located at corresponding positions, indicating the formation of bimetal alloy particles. In N-doped carbon/FeCoCu-15 (Fig. 1j), nitrogen is also integrated into the carbon matrix, and the Cu metal, combined with FeCo alloy, forms the large metal particle. The Cu and FeCo alloy domains within the metal particle in N-doped carbon/FeCoCu-15 were examined (Fig. 1f). Elemental mappings (Fig. S4†) of a single metal particle reveal a predominant presence of Cu, while Fe and Co are localized to a small region at the edges, consistent with the elemental mappings shown in Fig. 1j. In aberration-corrected HAADF–STEM images (Fig. 1g), the Cu metal shows an interplanar spacing of 0.210 nm, corresponding to the (111) facets with the space group $Fm\bar{3}m$. On the other hand, the FeCo alloy reveals a distorted cubic crystalline structure with interplanar spacings of 0.202 nm (associated with the (01-1) facets) and 0.235 nm (corresponding to the distorted (110) facets). These interplanar spacings align with the SAED patterns shown in Fig. 1h. The observed lattice distortion in FeCo alloy could result from lattice mismatch between Cu and FeCo during heteroepitaxial growth. High-resolution TEM images of graphitic nanotubes in N-doped carbon/FeCo and N-doped carbon/FeCoCu-15 (Fig. 1i) demonstrate a consistent d-spacing of 0.33 nm, corresponding to the (002) planes of graphite. However, the thickness of graphitic walls in N-doped carbon/FeCoCu-15 is reduced due to the enlarged particles encased within the nanotubes. In contrast, in N-doped carbon/FeCoCu-2 (Fig. S5a†) and N-doped carbon/FeCoCu-10 (Fig. S5b†), elemental mappings show the dispersed distribution of C, N, Fe, Co, and Cu without the formation of particles. Isolated single metal atoms dispersed throughout N-doped carbon/FeCoCu-2 and N-doped carbon/FeCoCu-10 are observed in HRTEM images (Fig. S6a and S7a†). The electron energy loss spectrum (EELS) confirms the coexistence of Fe and Co in N-doped carbon/FeCoCu-2 (Fig. S6b†), and Fe, Co and Cu in N-doped carbon. FeCoCu-10 (Fig. S7c and d†). In N-doped carbon/FeCoCu-20 (Fig. S5c†), dimensions of the metal particles have increased.

In Fig. 2a, XRD patterns for all samples show a broad peak at $26.4°$ (2θ), attributed to the (002) planes of graphitic carbon (PDF No. 01-0640). In N-doped carbon/FeCo, N-doped carbon/FeCoCu-15 and FeCoCu-20, a minor peak at $44.7°$ is observed, attributed to the (110) planes of cubic FeCo alloy (PDF No. 44-1433). In N-doped carbon/FeCoCu-15 and FeCuCo-20, specific peaks at $43.3°$, $50.4°$, and $74.0°$ are discerned and assigned to copper metal (PDF No. 03-1005). With the addition of excess Cu, a portion of Cu transforms into Cu_4N (PDF No. 47-1072), as evidenced by peaks at $41.2°$ and $47.9°$ in N-doped carbon/

FeCoCu-20. No discernible signals of metallic phases are detected in N-doped carbon/FeCoCu-2 and FeCoCu-10, which aligns with the TEM analysis. NMR spectra (Fig. 2b) were acquired to investigate the local environment and electronic property changes of Co after the introduction of Cu. In comparison to N-doped carbon/FeCo, the peaks shift downfield in N-doped carbon/FeCoCu-2 and N-doped carbon/FeCoCu-10, suggesting a deshielding effect on the Co protons likely due to the presence of electronegative atoms like N. This shift confirms the formation of single-atom Co–N–C bonding in low Cu concentration samples. Conversely, the peaks shift upfield in the N-doped carbon/FeCoCu-15 and FeCoCu-20, suggesting the impact of nearby electron-donating groups or the bonding of Co with Cu atoms. This effect could also contribute to the observed distorted d-spacings in the FeCo alloys present in N-doped carbon/FeCoCu-15. Additionally, surface defects are measured by the Raman spectra (Fig. 2c). The peaks centered at 1360, 1566, and 2855 cm^{-1} represent the typical D, G and 2D bands, respectively. All materials exhibit a moderately defective graphitic carbon structure, with I_D/I_G ratios around 1: N-doped carbon/FeCo (1.063), N-doped carbon/FeCoCu-2 (1.046), N-doped carbon/FeCoCu-10 (1.082), N-doped carbon/FeCoCu-15 (1.032), and N-doped carbon/FeCoCu-20 (1.034). Among them, N-doped carbon/FeCoCu-15 shows the lowest I_D/I_G value due to the enhanced formation of graphitic nanotubes within N-doped carbon/FeCoCu-15. The high degree of graphitization in carbon improves electronic conductivity, facilitating rapid electron transfer essential for efficient and effective catalytic activity.[54] The N_2 adsorption–desorption isotherms (Fig. 2d) indicate that N-doped carbon/FeCoCu-15 possesses the highest specific surface area at 228 m^2 g^{-1}, outperforming N-doped carbon/FeCo (187 m^2 g^{-1}), N-doped carbon/FeCoCu-2 (28 m^2 g^{-1}), N-doped carbon/FeCoCu-10 (98 m^2 g^{-1}), and N-doped carbon/FeCoCu-20 (194 m^2 g^{-1}). Barrett–Joyner–Halenda (BJH) pore size distribution curves (Fig. S8†) reveal the coexistence of micropores and mesopores in all samples. Notably, N-doped carbon/FeCoCu-15 presents an enhanced pore volume of 0.44 cm^3 g^{-1}, surpassing values of 0.34 cm^3 g^{-1} for N-doped carbon/FeCo, 0.13 cm^3 g^{-1} for N-doped carbon/FeCoCu-2, 0.24 cm^3 g^{-1} for N-doped carbon/FeCoCu-10, and 0.33 cm^3 g^{-1} for N-doped carbon/FeCoCu-20. Within N-doped carbon/FeCoCu-15, the FeCoCu metal nuclei catalyze the transformation of N-doped carbon into N-doped graphitic nanotubes, generating expansive tunnel spaces and increasing surface area as well as pore volume. Such improvements are beneficial for enhancing mass transfer at the catalyst/reactant/electrolyte multiphase interface and offering abundant active sites for electrocatalytic reactions.

The chemical compositions and their binding states were further investigated by XPS. The full survey spectra (Fig. S9†) validate the presence of Cu in N-doped carbon/FeCoCu samples. The elemental composition is provided in Table S1.† The fitted high-resolution N 1 s spectra for N-doped carbon/FeCo and N-doped carbon/FeCoCu samples (Fig. 3a) reveal the coexistence of five types of nitrogen species, pyridinic N (398.5 eV), metal-coordinated N (399.8 eV), pyrrolic N (400.9 eV), quaternary N (also referred to as graphitic N, 402.6 eV) and oxidized N (404.2 eV).[55] Both pyridinic- and metal-nitrogen
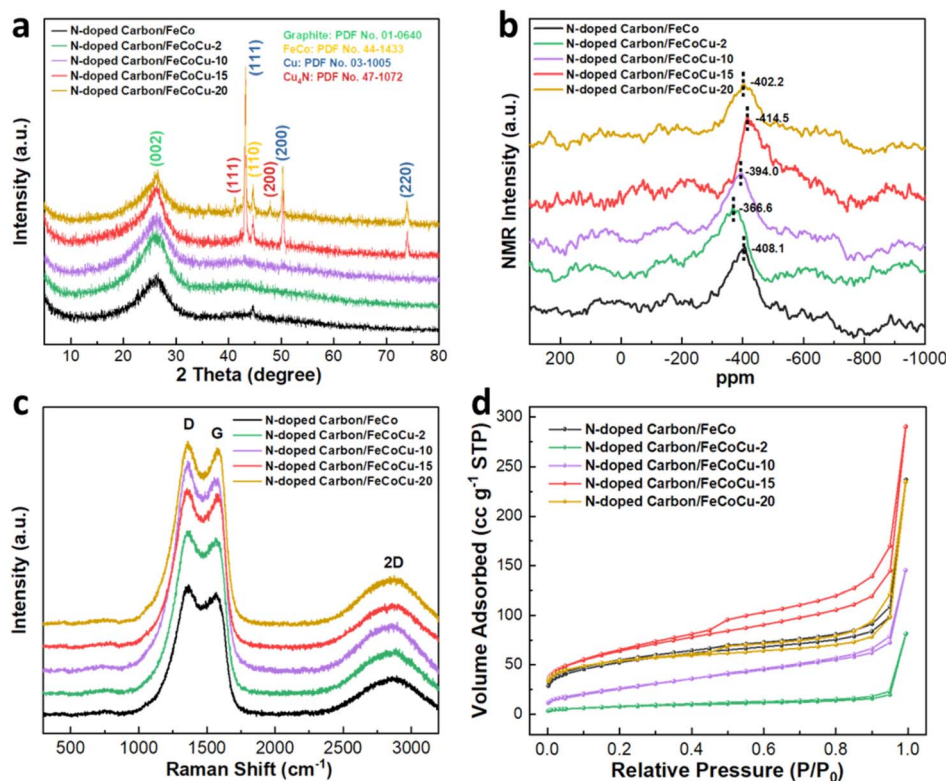
14220 | J. Mater. Chem. A, 2025, 13, 14216–14228

This journal is © The Royal Society of Chemistry 2025

Fig. 2 (a) XRD Patterns, (b) NMR Spectra, (c) Raman spectra, and (d) N$_2$ adsorption–desorption isotherms of as-prepared catalysts.

enhance electron donation and weaken the O–O bond by promoting oxygen bonding with nitrogen or adjacent carbon atoms, thereby serving as active sites to facilitate O$_2$ reduction.[8,23,37,56,57] N incorporation with C is also confirmed by the fitted high-resolution C 1s spectra (Fig. 3b), which can be deconvoluted into five peaks at the binding energies of 248.8,

286.1, 287.6, 289.2 and 290.9 eV, corresponding to C–C, C–N, C=O, –COO and π–π* respectively. The increased π–π* content observed in N-doped carbon/FeCoCu-15 in XPS is in line with its low I_D/I_G value in Raman spectra. The significant presence of C–N bonds in N-doped carbon/FeCoCu-15, along with the electron-donating effect of metal coordinated with N in
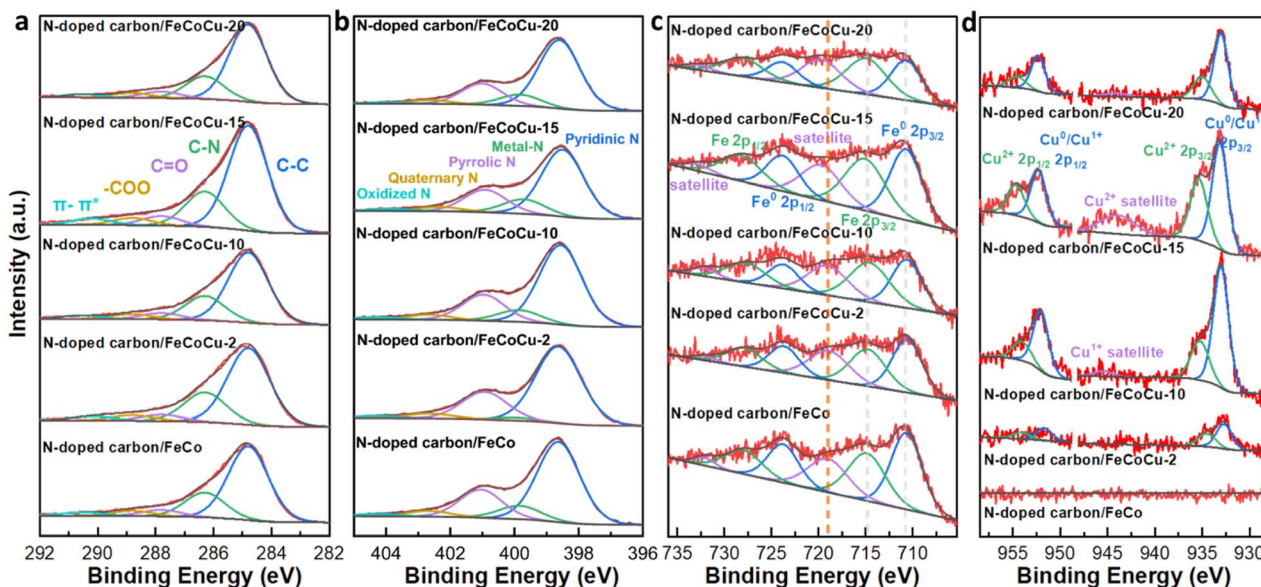

Fig. 3 High-resolution XPS spectra of (a) C 1s, (b) N 1s, (c) Fe 2p, and (d) Cu 2p for N-doped carbon/FeCo and N-doped carbon/FeCoCu samples.

metal–N–C moieties, can enhance the electron density of neighbouring C atoms, which is anticipated to enhance the adsorption of oxygen intermediates and facilitate electron transfer in ORR reactions.[35,36] In Fig. 3c, the deconvoluted Fe 2p spectra of all samples exhibit zero valence states at 710.7 eV and 723.8 eV, corresponding to metallic Fe in the FeCo alloy. For N-doped carbon/FeCo, N-doped carbon/FeCoCu-2, and N-doped carbon/FeCoCu-10, high-valence states are observed at 714.8 eV and 727.9 eV, along with satellites at 719.0 eV and 732.0 eV. Nevertheless, N-doped carbon/FeCoCu-15 and FeCoCu-20 exhibit a lower binding energy of oxidized Fe states (715.2 eV and 728.3 eV) with satellite features at 719.8 eV and 732.9 eV, suggesting a higher valence state of Fe in N-doped carbon/FeCoCu-15 and N-doped carbon/FeCoCu-20 compared to N-doped carbon/FeCo, N-doped carbon/FeCoCu-2, and N-doped carbon/FeCoCu-10. Similarly, for the N-doped carbon/FeCoCu samples, the Cu 2p spectra (Fig. 3d) can be deconvoluted into a low-valence state of Cu^0/Cu(I) at 932.7 eV and 952.6 eV, and Cu(II) at 934.9 eV and 954.8 eV. The shakeup satellite at 943.0 eV confirms the presence of a high valence state of Cu(II) species in N-doped carbon/FeCoCu-15 and FeCoCu-20, while N-doped carbon/FeCoCu-10 shows a weak satellite of Cu(I) at 944.3 eV.[58] In contrast, no Cu peak is observed for N-doped carbon/FeCo. The identification of high-valence Fe and Cu in the N-doped carbon/FeCoCu samples suggests that the carbon nanotubes enclosing FeCoCu nanoparticles have undergone partial oxidation as a result of electron transfer through metal–N–C moieties, consequently impacting the local environment and electronic structure of the catalysts.

3.2 Electrocatalytical characterization

The ORR performance of the prepared catalysts is evaluated using a rotating disk electrode (RDE) within a three-electrode cell with O_2-saturated 0.1 M KOH as the electrolyte, and the results are compared with commercial 20% Pt/C catalyst. The recording potential in 0.1 M KOH was referenced to the RHE potential through calibration. In CV curves (Fig. 4a), the oxygen reduction peak shifts positively with increasing Cu concentration from 2 mmol to 15 mmol but slightly reverses with a further increase to 20 mmol. The positive shift is attributed to the formation of FeCo alloy and Cu particles at a 15 mmol Cu precursor concentration, which promotes the formation of graphitic nanotubes and increases the specific surface area. However, excessive Cu precursor concentration (e.g., 20 mmol) results in FeCo alloy and Cu metal particle expansion, causing nanotube collapse. Additionally, exposure to N_2 transforms Cu metal partially into Cu_3N, collectively contributing to the negative shift in the reduction peak for N-doped carbon/FeCoCu-20. The reduction peak at 0.855 V for N-doped carbon/FeCoCu-15 is more positive compared to 0.826 V for N-doped carbon/FeCo and 0.824 V for Pt/C, demonstrating the exceptional ORR electrocatalytic activity of N-doped carbon/FeCoCu-15. LSV curves (Fig. 4b) were measured at a rotation speed of 1600 rpm with a scan rate of 10 mV s^{-1}. N-doped carbon/FeCoCu-15 demonstrates superior ORR activity with an elevated half-wave potential ($E_{1/2}$) of 0.852 V in contrast to N-

doped carbon/FeCo (0.820 V), N-doped carbon/FeCoCu-2 (0.800 V), N-doped carbon/FeCoCu-10 (0.815 V), N-doped carbon/FeCoCu-20 (0.839 V), and also outperforming the commercial Pt/C (0.808 V). Moreover, as illustrated in Fig. 4c, N-doped carbon/FeCoCu-15 exhibits an impressive kinetic current density of 16.44 mA cm^{-2} at 0.85 V, surpassing N-doped carbon/FeCo (2.80 mA cm^{-2}), N-doped carbon/FeCoCu-2 (0.77 mA cm^{-2}), N-doped carbon/FeCoCu-10 (1.86 mA cm^{-2}), N-doped carbon/FeCoCu-20 (6.49 mA cm^{-2}), as well as Pt/C (3.47 mA cm^{-2}). The superior kinetics of N-doped carbon/FeCoCu-15 is further validated by its smaller Tafel slope of 61.6 mV dec^{-1} (Fig. 4d), contrasting with N-doped carbon/FeCo (69.4 mV dec^{-1}) and Pt/C (73.0 mV dec^{-1}). Detailed comparisons of ORR activity and kinetics between N-doped carbon/FeCoCu catalysts and other nonprecious catalysts are provided in Table S6.† LSV curves were recorded at various rotation speeds to investigate the ORR pathway of N-doped carbon/FeCo and N-doped carbon/FeCoCu electrocatalysts. The parallel Koutecky–Levich (K–L) plots obtained from LSV curves suggest first-order reaction kinetics with respect to the dissolved O_2.[28,35] The electron-transfer number (n) is calculated to be 3.93–3.98 for N-doped carbon/FeCoCu-15 (Fig. 4e), suggesting a high-efficiency four-electron pathway for the ORR process. Similarly, an n value of 3.97–4.00 is attained for Pt/C (Fig. S11a and b†), while an n value of 3.89–3.96 is determined for N-doped carbon/FeCo (Fig. S11c and d†). The electron transfer properties of catalysts are evaluated via electrochemical impedance spectroscopy (EIS). In the Nyquist plots (Fig. 4f), N-doped carbon/FeCoCu-15 demonstrates a significantly smaller semicircle diameter, indicating reduced charge transfer resistance compared to Pt/C and other reference catalysts. The improved conductivity could lead to faster reaction kinetics. Moreover, N-doped carbon/FeCoCu-15 demonstrates exceptional stability, retaining 85.3% of the initial current in a chronoamperometry measurement at 0.45 V vs. RHE for 10 hours (Fig. 4g). This performance exceeds that of Pt/C (70.2%) and N-doped carbon/FeCo (79.3%). As depicted in Fig. 4h, after 10 hours of reaction, there is no noticeable decay in $E_{1/2}$ and only a minor negative shift in the CV reduction peak, whereas Pt/C exhibits a significant negative shift in both $E_{1/2}$ in LSV and the CV reduction peak (Fig. S13†), demonstrating the exceptional stability of N-doped carbon/FeCoCu-15. Furthermore, with the introduction of 3 M methanol, current–time curves (Fig. 4i) show a notable reduction in the oxygen reduction current at the Pt/C electrode, suggesting a negative crossover effect. In contrast, a slight decrease in current was noticed at the N-doped carbon/FeCoCu-15 electrode, indicating improved stability and selectivity for the ORR compared to Pt/C. The electrochemically active surface area (ECSA) was determined using electrochemical double-layer capacitance (C_{dl}). As depicted in Fig. S15,† the improved ECSA of N-doped carbon/FeCoCu-15 (10.4 mF cm^{-2}) is attributed to its expansive specific surface area, which offers numerous active sites for electrocatalytic reactions. The turnover frequency (TOF) was calculated to evaluate the intrinsic activity of the as-prepared catalysts and detailed calculations are provided in Table S7.† N-doped carbon/FeCoCu-15 exhibits a higher TOF of 0.017 s^{-1} compared to N-doped carbon/FeCo (0.016 s^{-1}) and commercial

14222 | J. Mater. Chem. A, 2025, 13, 14216–14228

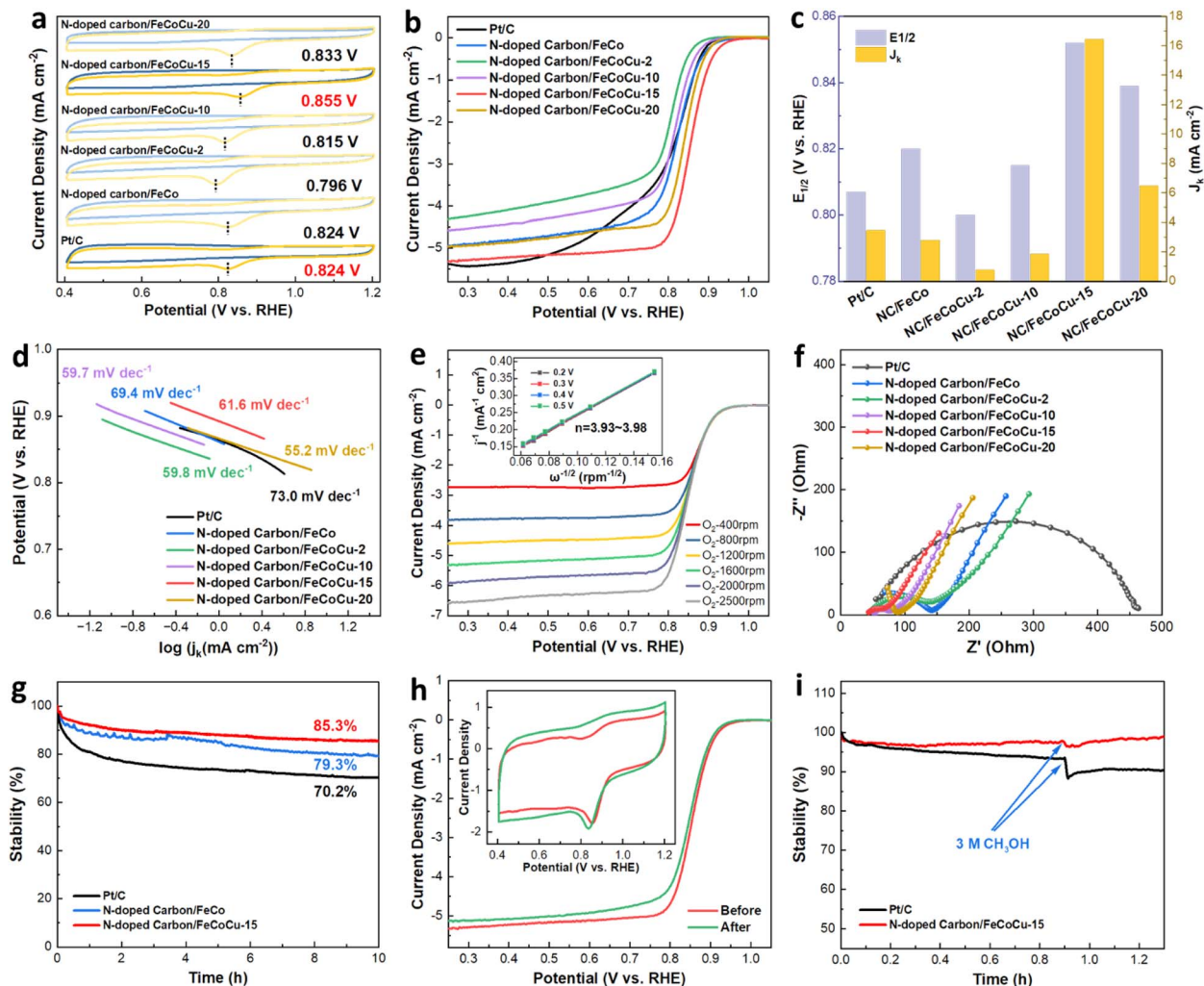This journal is © The Royal Society of Chemistry 2025

Fig. 4 (a) CV curves, (b) ORR LSV curves, (c) comparison of $E_{1/2}$ and kinetic current density (J_k) at 0.85 V, and (d) Tafel plots of Pt/C and as-prepared catalysts. (e) ORR LSV at different rotation speeds and corresponding K–L plots (inset) of N-doped carbon/FeCoCu-15. (f) Nyquist plots. (g) Chronoamperometry measurements for Pt/C, N-doped carbon/FeCo, and N-doped carbon/FeCoCu-15. (h) ORR LSV and CV curves of N-doped carbon/FeCoCu-15 before and after chronoamperometry test. (i) Chronoamperometry curves with the addition of 3 M methanol.

Pt/C (0.011 s^{-1}), indicating more efficient catalytic site utilization.[59] Additionally, OER activities of as-prepared catalysts were also measured in a 1.0 M KOH solution. Based on the LSV curves (Fig. S16†), N-doped carbon/FeCoCu-15 displays impressive OER catalytic activity, with a low overpotential of 430 mV at a current density of 10 mA cm^{-2}. This overpotential is significantly smaller than those observed for Pt/C, N-doped carbon/FeCo, N-doped carbon/FeCoCu-2, N-doped carbon/FeCoCu-10, and N-doped carbon/FeCoCu-20. In comparison, the state-of-the-art commercial OER catalyst, RuO$_2$, exhibits a lower onset potential and overpotential (320 mV) at a current density of 10 mA cm^{-2}, but a larger Tafel slope (103 mV dec^{-1}) than N-doped carbon/FeCoCu-15 (79 mV dec^{-1}).

3.3 DFT calculation

To gain further insights into the ORR catalytic mechanism of N-doped carbon/FeCoCu-15, first-principles calculations using density functional theory (DFT) methods were employed to analyze the electronic structure and catalytic reactions. Three structures were modeled for examination: FeCo alloy nanoparticles encapsulated in N-doped carbon nanotubes (NC/FeCo), individual Fe, Co, Cu atoms within N-doped carbon nanotubes (NC/Fe-Co-Cu), and FeCoCu nanoparticles enclosed in N-doped carbon nanotubes (NC/FeCoCu), as illustrated in Fig. S17.† The optimized geometry models for all catalysts are presented in Fig. 5a–c, which demonstrate a strong interaction and charge redistribution at the interface, with electron transfer from FeCoCu nanoparticles to N-doped carbon nanotubes. As shown in Fig. 5d, all three catalysts exhibit metallic characteristics, with the projected density of states (DOS) crossing the Fermi level. Notably, the electronic states near the Fermi level are significantly enhanced in N-doped carbon/FeCoCu compared to N-doped carbon/FeCo and N-doped carbon/Fe-Co-Cu, indicating improved electronic conductivity. The sharp peaks near the Fermi level in N-doped carbon/FeCoCu may result from hybridization between the 2p states of C atoms, the
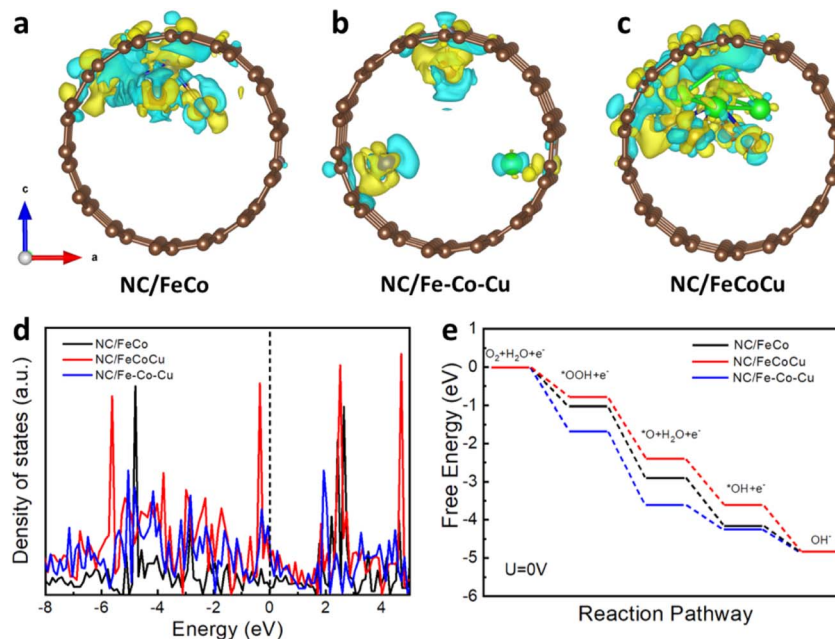
This journal is © The Royal Society of Chemistry 2025

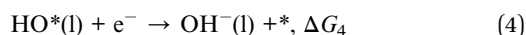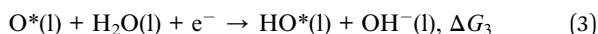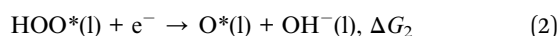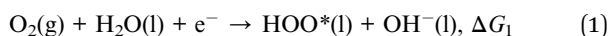*J. Mater. Chem. A*, 2025, **13**, 14216–14228 | **14223**

Fig. 5 The optimized geometry models of (a) N-doped carbon/FeCo, (b) N-doped carbon/Fe-Co-Cu, and (c) N-doped carbon/FeCoCu. Yellow regions indicate an increase in charge density and blue regions represent a decrease in charge density. (d) The projected density of states and (e) free-energy landscape of intermediates in the standard four electron transfer reaction pathway for ORR catalysis by the three electrocatalysts.

2p states of adjacent N atoms, and the 3d states of FeCoCu atoms. This is consistent with the XPS results, which indicate that FeCoCu nanoparticles have undergone partial oxidation due to electron transfer through metal–N–C moieties to the carbon materials. This electron transfer, along with N doping, introduces additional delocalized "electron-donating" areas.

Based on prior research and the electrocatalytic measurements presented above, the ORR follows the four-electron pathway in alkaline conditions. An associative mechanism that includes HOO* species in an alkaline environment progresses through the following elementary steps:[23]

$$O_2(g) + H_2O(l) + e^- \rightarrow HOO^*(l) + OH^-(l), \Delta G_1 \quad (1)$$

$$HOO^*(l) + e^- \rightarrow O^*(l) + OH^-(l), \Delta G_2 \quad (2)$$

$$O^*(l) + H_2O(l) + e^- \rightarrow HO^*(l) + OH^-(l), \Delta G_3 \quad (3)$$

$$HO^*(l) + e^- \rightarrow OH^-(l) + ^*, \Delta G_4 \quad (4)$$

where * represents an active site on the surface of the electrocatalyst, l and g denote the liquid and gas phases, respectively, and O*, OH*, and HOO* represent the adsorbed intermediates. All elementary reaction steps are exothermic, and the step with the least exergonicity within a specific reaction pathway is the rate-determining step that sets the limiting potential for ORR:

$$U_L \text{ (ORR)} = Mini[-\Delta G_i]/ne \quad (5)$$

Fig. 5e illustrates the free energies of adsorbed intermediates on N-doped carbon/FeCo, N-doped carbon/FeCoCu and N-doped carbon/Fe-Co-Cu at $U = 0$ V. The electron transfer steps in the ORR show a downhill trend, indicating exothermic reactions that can occur spontaneously. For N-doped carbon/FeCoCu, the smallest Gibbs free energy change among the four reaction steps suggests that the first step is the rate-limiting step in the ORR. In contrast, for N-doped carbon/FeCo and N-doped carbon/Fe-Co-Cu, the smallest ΔG_4 reveals that the rate-limiting step occurs during the fourth electron transfer reaction. Specifically, the U_L(ORR) values for the rate-limiting steps are determined to be 0.79 eV for N-doped carbon/FeCo-Cu, 0.68 eV for N-doped carbon/FeCo, and 0.59 eV for N-doped carbon/Fe-Co-Cu, thus the catalytic ORR performance follows the trend: N-doped carbon/Fe-Co-Cu < N-doped carbon/FeCo < N-doped carbon/FeCoCu. The electron-donating characteristics of FeCoCu nanoparticles and nitrogen doping can enhance the adsorption of intermediates onto the carbon surface while weakening the binding of adsorbed OH⁻ products, effectively improving the efficiency of electron transfer reactions. Therefore, the DFT calculations align well with the experimental results, revealing the synergetic coupling between FeCoCu nanoparticles and N-doped carbon, which creates a favorable surface electronic environment and enhances the ORR performance.

3.4 Electrochemical performance of ZABs

Two-electrode aqueous zinc–air batterie were assembled to evaluate the electrocatalytical performance of as-prepared catalysts. In this setup (Fig. 6a), the air cathode functions as a bifunctional electrode, catalyzing both ORR and OER under alternating discharge and charge potentials. Inspired by the favorable OER activity of N-doped carbon/FeCoCu-15, its performance as a bifunctional catalyst was first evaluated in
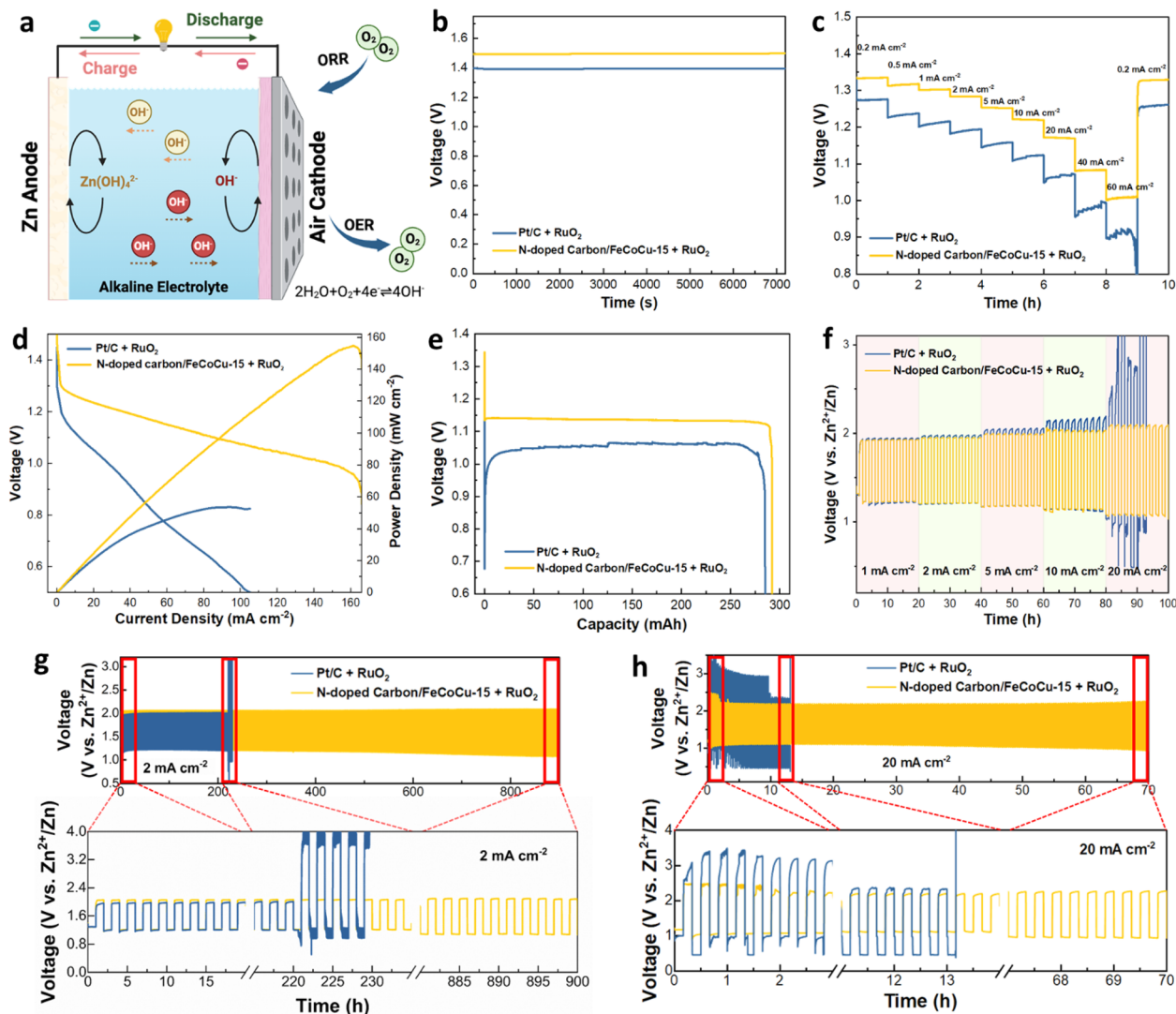
14224 | J. Mater. Chem. A, 2025, 13, 14216–14228

This journal is © The Royal Society of Chemistry 2025

Fig. 6 (a) Schematic illustration of zinc–air batteries. (b) Open-circuit voltage, (c) discharge voltages at various current densities, (d) discharge polarization curves, (e) discharge curves, (f) galvanostatic cycling at current densities of 1, 2, 5, 10, and 20 mA cm^{-2}, (g) long-term galvanostatic cycling at 2 mA cm^{-2} and (h) long-term galvanostatic cycling at 20 mA cm^{-2} of zinc–air batteries based on Pt/C and N-doped carbon/FeCoCu-15 ORR electrocatalysts.

zinc–air coin cells. N-doped carbon/FeCoCu-15 was exclusively coated on carbon paper, serving as the air cathode, with zinc foil acting as the anode and 6 M KOH + 0.2 M ZnCl$_2$ as the electrolyte. 6 M KOH electrolyte is utilized to ensure a high ionic conductivity and suppress hydrogen evaluation at the surface of Zn metal.[19] 0.2 M zinc chloride is added to KOH electrolyte to increase the rechargeable performance of Zn–air batteries.[22,60–63] Galvanostatic cycling was performed to assess the rechargeability of zinc–air coin cells (Fig. S18†). The assembled coin cell with only N-doped carbon/FeCoCu-15 in air cathode exhibits a lifespan of 10 cycles over a period of 3 hours at a moderate current density of 2 mA cm^{-2}, indicating unsatisfactory rechargeability. However, when combined with commercial RuO$_2$ as the OER catalyst, a coin cell with hybrid cathode of N-doped carbon/FeCoCu-15 and RuO$_2$ demonstrated the ability to charge and discharge for more than 42 cycles over 14 hours. The

rechargeability of batteries is greatly improved by adding an OER catalyst. However, in coin cells, the rapid deterioration of zinc–air batteries could be attributed to the passivation of the Zn anode. The passivation process involves the accumulation of saturated Zn(OH)$_4^{2-}$ and the precipitation of ZnO on the surface, acting as a diffusion barrier for OH$^-$ ions and leading to increased resistance in the zinc anode.[10,64] The flow electrolyte system proves to be a highly effective method for zinc–air batteries.[65] Besides removing precipitated by-products, the flow electrolyte enhances OH$^-$ transfer and minimizes concentration gradients at the electrodes. A homemade rechargeable zinc–air flow battery was assembled with electrolyte actively pumped and circulated through the cell using an external pump. N-doped carbon/FeCoCu-15, functioning as the ORR catalyst, and commercial RuO$_2$, serving as the OER catalyst, were mixed and coated on the carbon cloth with a loading

This journal is © The Royal Society of Chemistry 2025

J. Mater. Chem. A, 2025, 13, 14216–14228 | **14225**

of 0.5 mg cm^{-2}, respectively. A hybrid air cathode with a mixture of Pt/C and RuO$_2$ was used as the control cathode in the battery to compare their performance. As shown in Fig. 6b, the N-doped carbon/FeCoCu-15 battery displays a higher open-circuit voltage of 1.50 V compared with the Pt/C battery (1.39 V). In the galvanostatic discharge curves (Fig. 6c), N-doped carbon/FeCoCu-15 shows higher discharging voltages, such as 1.33 V at 0.2 mA cm^{-2}, 1.30 V at 1.0 mA cm^{-2}, 1.25 V at 5 mA cm^{-2}, 1.17 V at 20 mA cm^{-2}, and 1.00 V at 60 mA cm^{-2}, compared to Pt/C (1.27 V at 0.2 mA cm^{-2}, 1.21 V at 1.0 mA cm^{-2}, 1.15 V at 5 mA cm^{-2}, 1.06 V at 20 mA cm^{-2}, and a dramatic drop of voltage at 60 mA cm^{-2}). This difference suggests higher efficiency of N-doped carbon/FeCoCu-15 battery during the discharging process, enabling the battery to operate at high power densities. The discharge polarization curves in Fig. 6d reveal that the maximum power density of N-doped carbon/FeCoCu-15 batteries reaches as high as 154.7 mW cm^{-2} at a high current density of 162 mA cm^{-2}, outperforming that of Pt/C batteries (53.7 mW cm^{-2} at 92.7 mA cm^{-2}). Remarkably, N-doped carbon/FeCoCu-15 battery delivered a specific capacity of 810 mA h g^{-1} at the discharge current density of 20 mA cm^{-2} with a corresponding energy density of 918 W h kg^{-1}, higher than that of Pt/C (800 mA h g^{-1}) with an energy density of 841 W h kg^{-1} (Fig. 6e). Meanwhile, N-doped carbon/FeCoCu-15 battery exhibits a negligible voltage drop of 6 mV, whereas the Pt/C battery experiences a large voltage drop of 377 mV. This drop is attributed to the large internal resistance of the Pt/C battery, including both diffusion resistance (R_d) and ohmic resistance (R_{ohm}), which is the aggregate of ionic resistance in the electrolyte, electronic resistance in active materials, and contact resistance between the active mass and current collector.[66] As depicted in Fig. 6f, the N-doped carbon/FeCoCu-15 battery demonstrates smaller voltage gaps and more stable charge–discharge curves compared to the Pt/C battery at various current densities ranging from 1 to 20 mA cm^{-1}. This distinction is particularly evident at the high current density of 20 mA cm^{-1}. The rechargeability and cyclic durability of catalysts are of great significance for the practical applications of Zn–air batteries. Long-term cycling tests were performed at current densities of 2 mA cm^{-2} and 20 mA cm^{-2}. As illustrated in Fig. 6g, in contrast to the Pt/C battery experiencing battery crash after 220 hours, the N-doped carbon/FeCoCu-15 battery shows minimal variation in voltage even after 450 charge/discharge cycles (equivalent to 900 h), indicating its remarkable long-term stability. At an elevated current density of 20 mA cm^{-2} (Fig. 6h), the Pt/C battery fails in the second cycle. In contrast, the N-doped carbon/FeCoCu-15 battery maintains a discharge voltage of 1.05 V and a charge voltage of 2.45 V in the second cycle. The initial voltage gap of 1.40 V decreases and stabilizes to 1.07 V in the following cycles, allowing the battery to operate for over 70 hours, showcasing exceptional stability. A high current density leads to increased overpotential, particularly in the OER process, and could induce the oxidation of the catalyst. The enhanced durability of N-doped carbon/FeCoCu-15 catalyst impedes the degradation process during charge and discharge cycles in zinc–air batteries. The performance comparison between the as-prepared and reported Zn–air batteries is listed in Table S8.†

4. Conclusions

In summary, a trinary N-doped carbon/FeCoCu electrocatalyst was successfully synthesized through pyrolysis and carbonization. By carefully adjusting the Cu content, the electrocatalytic ORR performance was optimized for N-doped carbon/FeCoCu-15, which demonstrated high electrocatalytic activity, with a porous hierarchical structure that promotes efficient mass transport, and a large specific surface area providing abundant active sites. DFT calculations further confirmed the enhancement of conductivity and the favourable surface electronic environment induced by FeCoCu nanoparticles and nitrogen doping in the carbon matrix. The delocalized electron-donating regions on the carbon surface facilitate oxygen bonding with carbon atoms and weaken the interaction with OH$^-$ products, thereby enhancing the reaction kinetics of ORR. In a practical application, the N-doped carbon/FeCoCu catalyst was integrated as an effective air cathode in a zinc–air battery, exhibiting superior rechargeability and long-term stability. This work opens new opportunities for optimizing noble-metal-free catalysts to achieve high-efficiency, stable electrocatalysts for metal-air batteries and other renewable energy systems.

Data availability

The authors confirm that the data supporting the findings of this study are available within the article and its ESI.†

Author contributions

Wen Zhao: conceptualization, methodology, investigation, formal analysis, data curation, validation, writing – original draft, writing – review & editing. Tianli Wu: methodology, data curation, software, writing – review & editing. Inosh Prabasha Perera: data curation, formal analysis, investigation. Yanliu Dang: formal analysis. Isaac T Olowookere: investigation. Qiang Luo: investigation. Haiyan Tan: formal analysis. Dilshan Silva: investigation. Steven L. Suib: funding acquisition, project administration, supervision, writing – review & editing.

Conflicts of interest

There are no conflicts to declare.

Acknowledgements

Notes and references

1 W. Sun, F. Wang, B. Zhang, M. Zhang, V. Küpers, X. Ji, C. Theile, P. Bieker, K. Xu, C. Wang and M. Winter, *Science*, 2021, **371**, 46–51.

14226 | *J. Mater. Chem. A*, 2025, **13**, 14216–14228

This journal is © The Royal Society of Chemistry 2025

2 Y. Li, M. Gong, Y. Liang, J. Feng, J. E. Kim, H. Wang, G. Hong, B. Zhang and H. Dai, *Nat. Commun.*, 2013, **4**, 1–7.

3 H. Pourzolfaghar, S. Hosseini, F. M. Zuki, M. Alinejad and Y. Y. Li, *Mater. Today Commun.*, 2021, **29**, 102954.

4 T. Cui, Y. P. Wang, T. Ye, J. Wu, Z. Chen, J. Li, Y. Lei, D. Wang and Y. Li, *Angew. Chem., Int. Ed.*, 2022, **61**, 202115219.

5 X. Hao, Z. Jiang, B. Zhang, X. Tian, C. Song, L. Wang, T. Maiyalagan, X. Hao and Z. J. Jiang, *Advanced Science*, 2021, **8**, 1–14.

6 N. Khodayar, A. Noori, M. S. Rahmanifar, M. Moloudi, N. Hassani, M. Neek-Amal, M. F. El-Kady, N. B. Mohamed, X. Xia, Y. Zhang, R. B. Kaner and M. F. Mousavi, *Energy Environ. Sci.*, 2024, **17**, 5200–5215.

7 Q. Liu, L. Wang and H. Fu, *J. Mater. Chem. A*, 2023, **11**, 4400–4427.

8 C. Y. Su, H. Cheng, W. Li, Z. Q. Liu, N. Li, Z. Hou, F. Q. Bai, H. X. Zhang and T. Y. Ma, *Adv. Energy Mater.*, 2017, **7**, 1602420.

9 J. S. Lee, S. T. Kim, R. Cao, N. S. Choi, M. Liu, K. T. Lee and J. Cho, *Adv. Energy Mater.*, 2011, **1**, 34–50.

10 P. Chen, K. Zhang, D. Tang, W. Liu, F. Meng, Q. Huang and J. Liu, *Front. Chem.*, 2020, **8**, 1–7.

11 T. Zhou, N. Zhang, C. Wu and Y. Xie, *Energy Environ. Sci.*, 2020, **13**, 1132–1153.

12 J. Zhang, Z. Zhao, Z. Xia and L. Dai, *Nat. Nanotechnol.*, 2015, **10**, 444–452.

13 F. Gu, W. Guo, Y. Yuan, Y. P. Deng, H. Jin, J. Wang, Z. Chen, S. Pan, Y. Chen and S. Wang, *Adv. Mater.*, 2024, 202313096.

14 S. Chen, H. Ren, Y. Qiu, C. Luo, Q. Zhao and W. Yang, *J. Power Sources*, 2023, **573**, 233116.

15 P. Chen, T. Zhou, L. Xing, K. Xu, Y. Tong, H. Xie, L. Zhang, W. Yan, W. Chu, C. Wu and Y. Xie, *Angew. Chem., Int. Ed.*, 2017, **56**, 610–614.

16 H. Cheng, M. L. Li, C. Y. Su, N. Li and Z. Q. Liu, *Adv. Funct. Mater.*, 2017, **27**, 1–10.

17 M. Gopalakrishnan, W. Kao-Ian, M. Rittiruam, S. Praserthdam, P. Praserthdam, W. Limphirat, M. T. Nguyen, T. Yonezawa and S. Kheawhom, *ACS Appl. Mater. Interfaces*, 2024, **16**, 11537–11551.

18 J. Balamurugan, P. M. Austeria, J. B. Kim, E. S. Jeong, H. H. Huang, D. H. Kim, N. Koratkar and S. O. Kim, *Adv. Mater.*, 2023, **35**, 2302625.

19 J. Pan, Y. Y. Xu, H. Yang, Z. Dong, H. Liu and B. Y. Xia, *Advanced Science*, 2018, **5**, 1700691.

20 X. Liu, L. Wang, P. Yu, C. Tian, F. Sun, J. Ma, W. Li and H. Fu, *Angew. Chem., Int. Ed.*, 2018, **57**, 16166–16170.

21 C. Guan, A. Sumboja, H. Wu, W. Ren, X. Liu, H. Zhang, Z. Liu, C. Cheng, S. J. Pennycook and J. Wang, *Adv. Mater.*, 2017, **29**, 1–9.

22 V. Jose, J. M. V. Nsanzimana, H. Hu, J. Choi, X. Wang and J. M. Lee, *Adv. Energy Mater.*, 2021, **11**, 2100157.

23 R. Ma, G. Lin, Y. Zhou, Q. Liu, T. Zhang, G. Shan, M. Yang and J. Wang, *npj Comput. Mater.*, 2019, **5**, 78.

24 W. Niu, S. Pakhira, K. Marcus, Z. Li, J. L. Mendoza-Cortes and Y. Yang, *Adv. Energy Mater.*, 2018, **8**, 1–11.

25 J. Han, H. Bao, J. Q. Wang, L. Zheng, S. Sun, Z. L. Wang and C. Sun, *Appl. Catal., B*, 2021, **280**, 119411.

26 Y. Tian, X. Liu, L. Xu, D. Yuan, Y. Dou, J. Qiu, H. Li, J. Ma, Y. Wang, D. Su and S. Zhang, *Adv. Funct. Mater.*, 2021, **31**, 202101239.

27 Y. Guo, P. Yuan, J. Zhang, H. Xia, F. Cheng, M. Zhou, J. Li, Y. Qiao, S. Mu and Q. Xu, *Adv. Funct. Mater.*, 2018, **28**, 1–9.

28 Y. Chen, S. Ji, S. Zhao, W. Chen, J. Dong, W. C. Cheong, R. Shen, X. Wen, L. Zheng, A. I. Rykov, S. Cai, H. Tang, Z. Zhuang, C. Chen, Q. Peng, D. Wang and Y. Li, *Nat. Commun.*, 2018, **9**, 5422.

29 T. Wang, Z. Kou, S. Mu, J. Liu, D. He, I. S. Amiinu, W. Meng, K. Zhou, Z. Luo, S. Chaemchuen and F. Verpoort, *Adv. Funct. Mater.*, 2018, **28**, 1–9.

30 Y. Xu, P. Deng, G. Chen, J. Chen, Y. Yan, K. Qi, H. Liu and B. Y. Xia, *Adv. Funct. Mater.*, 2020, **30**, 1–8.

31 Y. Guo, P. Yuan, J. Zhang, Y. Hu, I. S. Amiinu, X. Wang, J. Zhou, H. Xia, Z. Song, Q. Xu and S. Mu, *ACS Nano*, 2018, **12**, 1894–1901.

32 Y. Wang, J. Wu, S. Tang, J. Yang, C. Ye, J. Chen, Y. Lei and D. Wang, *Angew. Chem., Int. Ed.*, 2023, **62**, 202219191.

33 H. W. Go, T. T. Nguyen, Q. P. Ngo, R. Chu, N. H. Kim and J. H. Lee, *Small*, 2023, **19**, 202206341.

34 J. Zhang, Z. Xia and L. Dai, *Sci. Adv.*, 2015, **1**, 1500564.

35 H. Jiang, J. Gu, X. Zheng, M. Liu, X. Qiu, L. Wang, W. Li, Z. Chen, X. Ji and J. Li, *Energy Environ. Sci.*, 2019, **12**, 322–333.

36 X. Ning, Y. Li, J. Ming, Q. Wang, H. Wang, Y. Cao, F. Peng, Y. Yang and H. Yu, *Chem. Sci.*, 2019, **10**, 1589–1596.

37 J. H. Wee, C. H. Kim, H. S. Lee, G. B. Choi, D. W. Kim, C. M. Yang and Y. A. Kim, *Sci. Rep.*, 2019, **9**, 1–7.

38 Q. D. Ruan, R. Feng, J. J. Feng, Y. J. Gao, L. Zhang and A. J. Wang, *Small*, 2023, **19**, 2300136.

39 L. Yan, H. Wang, J. Shen, J. Ning, Y. Zhong and Y. Hu, *Chem. Eng. J.*, 2021, **403**, 126385.

40 Z. Wang, J. Ang, B. Zhang, Y. Zhang, X. Y. D. Ma, T. Yan, J. Liu, B. Che, Y. Huang and X. Lu, *Appl. Catal., B*, 2019, **254**, 26–36.

41 J. Yu, *Chin. Sci. Bull.*, 2021, **66**, 1542–1543.

42 Q. Jing, Z. Mei, X. Sheng, X. Zou, Y. Yang, C. Zhang, L. Wang, Y. Sun, L. Duan and H. Guo, *Chem. Eng. J.*, 2023, **462**, 142321.

43 Y. P. Deng, Y. Jiang, R. Liang, N. Chen, W. Chen, Z. W. Yin, G. King, D. Su, X. Wang and Z. Chen, *J. Am. Chem. Soc.*, 2023, **145**, 20248–20260.

44 Y. Yu, P. Rao, S. Feng, M. Chen, P. Deng, J. Li, Z. Miao, Z. Kang, Y. Shen and X. Tian, *Acta Phys. Chim. Sin.*, 2023, **39**, 2210039.

45 C. Wu, Y. Yu, Y. Song, P. Rao, X. Han, Y. Liang, J. Li, K. Zhang, Z. Zhang, P. Deng, X. Tian and D. Wu, *J. Energy Chem.*, 2025, **104**, 472–481.

46 M. Guo, X. Zhang, T. Yang, Q. Dang, X. Li, Y. Wang and G. Zhang, *J. Power Sources*, 2020, **456**, 227933.

47 A. Adhikari, K. Chhetri, R. Rai, D. Acharya, J. Kunwar, R. M. Bhattarai, R. K. Jha, D. Kandel, H. Y. Kim and M. R. Kandel, *Nanomaterials*, 2023, **12**, 2612.

48 L. Chen, Y. Zhang, L. Dong, W. Yang, X. Liu, L. Long, C. Liu, S. Dong and J. Jia, *J. Mater. Chem. A*, 2020, **8**, 4369–4375.

49 V. Jose, H. Hu, E. Edison, W. Manalastas, H. Ren, P. Kidkhunthod, S. Sreejith, A. Jayakumar,

This journal is © The Royal Society of Chemistry 2025

J. Mater. Chem. A, 2025, **13**, 14216–14228 | 14227

J. M. V. Nsanzimana, M. Srinivasan, J. Choi and J. M. Lee, *Small Methods*, 2023, **12**, 2612.

50 W. Zhang, B. Feng, L. Huang, Y. Liang, J. Chen, X. Li, Z. Shi and N. Wang, *Appl. Catal., B*, 2024, **385**, 124450.

51 D. Joubert, *Phys. Rev. B:Condens. Matter Mater. Phys.*, 1999, **59**, 1758–1775.

52 L. Xiao, Y. Li, P. Yang, Q. Lv, X. Lu, H. Xu, R. Li, H. Zhang, S. Yang, A. Liu, D. Wang, J. Zhang and M. An, *J. Power Sources*, 2025, **632**, 236360.

53 T. Moriai, T. Tsukamoto, K. Fukuhara, T. Imaoka, T. Kambe and K. Yamamoto, *Nanoscale Adv.*, 2025, **7**, 346–353.

54 Q. Lu, H. Wu, X. Zheng, Y. Chen, A. L. Rogach, X. Han, Y. Deng and W. Hu, *Advanced Science*, 2021, **8**, 1–10.

55 R. Li, D. Wu, P. Rao, P. Deng, J. Li, J. Luo, W. Huang, Q. Chen, Z. Kang, Y. Shen and X. Tian, *Carbon Energy*, 2023, **5**, e294.

56 M. B. Poudel, S. Vijayapradeep, K. Sekar, J. S. Kim and D. J. Yoo, *J. Mater. Chem. A*, 2024, **12**, 10185–10195.

57 M. B. Poudel, M. P. Balanay, P. C. Lohani, K. Sekar and D. J. Yoo, *Adv. Energy Mater.*, 2024, **30**, 2400347.

58 M. C. Biesinger, L. W. M. Lau, A. R. Gerson and R. S. C. Smart, *Appl. Surf. Sci.*, 2010, **257**, 887–898.

59 M. R. Subramaniam, S. Ramakrishnan, S. Sidra, S. C. Karthikeyan, S. Vijayapradeep, J. Huang, M. Mamlouk, D. H. Kim and D. J. Yoo, *J. Mater. Chem. A*, 2024, **12**, 5967–5979.

60 C. Tang, B. Wang, H. F. Wang and Q. Zhang, *Adv. Mater.*, 2017, **29**, 1–7.

61 H. Bin Yang, J. Miao, S. F. Hung, J. Chen, H. B. Tao, X. Wang, L. Zhang, R. Chen, J. Gao, H. M. Chen, L. Dai and B. Liu, *Sci. Adv.*, 2016, **2**, 1–12.

62 G. Fu, Z. Cui, Y. Chen, Y. Li, Y. Tang and J. B. Goodenough, *Adv. Energy Mater.*, 2017, **7**, 1–8.

63 L. Yan, Z. Xu, W. Hu, J. Ning, Y. Zhong and Y. Hu, *Nano Energy*, 2021, **82**, 105710.

64 J. Fu, Z. P. Cano, M. G. Park, A. Yu, M. Fowler and Z. Chen, *Adv. Mater.*, 2017, **29**, 1604685.

65 K. Wu, L. Zhang, Y. Yuan, L. Zhong, Z. Chen, X. Chi, H. Lu, Z. Chen, R. Zou, T. Li, C. Jiang, Y. Chen, X. Peng and J. Lu, *Adv. Mater.*, 2020, **32**, 1–9.

66 T. Kowitkulkrai, A. Kaewpradap, S. Hirai, V. Lailuck, S. Rompho and M. Masomtob, *IOP Conf. Ser.:Mater. Sci. Eng.*, 2019, **501**, 012057.